Radio continuum observations of Class I protostellar discs in Taurus: constraining the greybody tail at centimetre wavelengths[⋆]

AMI Consortium: Anna M. M. Scaife,[1,2]† Jane V. Buckle,[3,4] Rachael E. Ainsworth,[2] Matthew Davies,[3] Thomas M. O. Franzen,[3,5] Keith J. B. Grainge,[3,4] Michael P. Hobson,[3] Natasha Hurley-Walker,[3,6] Anthony N. Lasenby,[3,4] Malak Olamaie,[3] Yvette C. Perrott,[3] Guy G. Pooley,[3] Tom P. Ray,[2] John S. Richer,[3,4] Carmen Rodríguez-Gonzálvez,[3] Richard D. E. Saunders,[3,4] Michel P. Schammel,[3] Paul F. Scott,[3] Timothy Shimwell,[3] David Titterington[3] and Elizabeth Waldram[3]

[1]*School of Physics & Astronomy, University of Southampton, Highfield, Southampton SO17 1BJ*
[2]*Dublin Institute for Advanced Studies, 31 Fitzwilliam Place, Dublin 2, Ireland*
[3]*Astrophysics Group, Cavendish Laboratory, J J Thomson Avenue, Cambridge CB3 0HE*
[4]*Kavli Institute for Cosmology, Cambridge, Madingley Road, Cambridge CB3 0HA*
[5]*CSIRO Astronomy & Space Science, Australia Telescope National Facility, PO Box 76, Epping, NSW 1710, Australia*
[6]*International Centre for Radio Astronomy Research, Curtin Institute of Radio Astronomy, 1 Turner Avenue, Technology Park, Bentley, WA 6845, Australia*

ABSTRACT

We present deep 1.8 cm (16 GHz) radio continuum imaging of seven young stellar objects in the Taurus molecular cloud. These objects have previously been extensively studied in the submm to near-infrared range and their spectral energy distributions modelled to provide reliable physical and geometrical parameters. We use these new data to constrain the properties of the long-wavelength tail of the greybody spectrum, which is expected to be dominated by emission from large dust grains in the protostellar disc. We find spectra consistent with the opacity indices expected for such a population, with an average opacity index of $\beta = 0.26 \pm 0.22$ indicating grain growth within the discs. We use spectra fitted jointly to radio and submm data to separate the contributions from thermal dust and radio emission at 1.8 cm and derive disc masses directly from the cm-wave dust contribution. We find that disc masses derived from these flux densities under assumptions consistent with the literature are systematically higher than those calculated from submm data, and meet the criteria for giant planet formation in a number of cases.

Key words: radiation mechanisms: general – stars: formation – ISM: clouds – ISM: general.

1 INTRODUCTION

The growth of dust grains from sub-µm to µm sizes in the local environment of protostellar objects is well probed by observational data in the mid-infrared (MIR); however, the further growth of these grains to larger sizes is only probed by their submm and cm-wave emission. It is this growth, and the possible coagulation and sedimentation that follows it, which is widely thought to lead to the formation of protoplanetary objects in the dense discs around evolving protostars. Measuring the long-wavelength tail of the thermal emission from dust, which is expected to be dominated by such large dust grains, often referred to as *pebbles*, provides an independent measure of the dust composition in the disc through its opacity index (β), as well as the mass of the accumulated matter in the disc which is an important factor in models of planet formation (e.g. Boss 1998).

Submm measurements towards circumstellar discs are often used to determine their potential for planet formation, as longer wavelength information provides a unique perspective on the cooler dust in the outer part of the disc. It is this region where protoplanets are expected to form. Alternative methods of disc mass estimation, such as spectral line measurements of molecular gas, are complicated by opacity effects (e.g. Beckwith & Sargent 1993) and require complex models to account for these effects as well as those of depletion (Dutrey, Guilloteau & Simon 2003; Kamp & Dullemond 2004).

[⋆]We request that any reference to this paper cites 'AMI Consortium: Scaife et al. 2011'.

†E-mail: a.scaife@soton.ac.uk

Table 1. AMI-LA sample of Class I protostars in Taurus. Column 1: source name; column 2: alternative designations for the source; column 3: source RA; column 4: source Dec.; column 5: major axis of the AMI-LA point spread function (PSF) in the combined channel image; column 6: minor axis of the AMI-LA PSF in the combined channel image; column 7: noise on the combined channel image; column 8: date of observation; column 9: primary (flux) calibrator source; column 10: secondary (phase) calibrator source.

Name	Other names	RA (J2000) ($^{\mathrm{h\,m\,s}}$)	Dec. (J2000) ($°\,'\,''$)	θ_{maj} (arcsec)	θ_{min} (arcsec)	σ_{rms} (μJy beam^{-1})	Date (dd-mm-yy)	Flux cal.	Phase cal.
IRAS 04016+2610	L1489 IRS	04 04 42.9	+26 19 02	38.9	24.6	23	26-03-11	3C 147	J0406+2728
DG Tau B		04 27 02.6	+26 05 31	32.9	21.6	27	07-07-11	3C 48	J0429+2724
IRAS 04248+2612	HH 31	04 27 57.3	+26 19 19	33.7	22.1	25	28-03-11	3C 147	J0429+2724
IRAS 04302+2247		04 33 16.5	+22 53 21	33.5	21.5	32	04-04-11	3C 147	J0438+2153
IRAS 04325+2402	L1535 IRS	04 35 35.4	+24 08 19	33.4	23.1	22	15-04-11	3C 48	J0438+2153
IRAS 04361+2547	TMR 1	04 39 13.9	+25 53 21	33.6	22.2	30	18-04-11	3C 48	J0440+2728
IRAS 04368+2557	L1527	04 39 53.6	+26 03 06	32.2	22.6	30	19-04-11	3C 48	J0440+2728

Submm and radio measurements are useful not only as a probe of the disc mass itself, but, with multiwavelength data available, they can also be used to determine the evolution of the opacity index as a function of frequency (Shirley et al. 2011a,b) and place constraints on the growth of dust grains in such discs. This can be used to determine whether the time-scales assumed in current models of planet formation are consistent with observational data. However, to date the disc masses determined from submm data appear to be too low to agree with theoretical models of planet formation (see e.g. Andrews & Williams 2005, hereafter AW05), although there are a number of observational caveats associated with these data.

In practice, multiple frequencies are required to constrain the properties of dust emission and draw comparisons with models of radiative transfer (Shirley et al. 2011a). In the submm, the observational properties of the dust derived from its spectral energy distribution (SED) can have contributions from both the envelope and the disc, which need to be separated. In order to probe the properties of the disc alone, it is necessary to go to longer wavelengths in order to ensure that it provides the dominant contribution to the SED. However, this transition regime, between the cm and submm wavelengths, is often confused by the presence of multiple emission processes each contributing to the overall SED. For younger protostellar objects, such as Class 0 sources, (partially) optically thin free–free emission is frequently observed to dominate the cm-wave spectrum; for Class I and II objects, the high magnetic field strength on the surface of the central star can lead to gyrosynchrotron emission from quasi-relativistic or thermal plasma.

In this work, we present SEDs for eight Class I protostars in the Taurus molecular cloud. These objects were selected from the sample of Gramajo et al. (2010) who used multifrequency data from MIR to submm wavelengths to model the SEDs of these objects. We here extend these SEDs to the cm-wave regime with the Arcminute Microkelvin Imager Large Array (AMI-LA) in order to constrain the long-wavelength properties of the optically thin emission expected to be dominated by their circumstellar discs.

2 OBSERVATIONS

AMI comprises two synthesis arrays, one of 10 3.7-m antennas (Small Array) and one of eight 13-m antennas (LA), both sited at the Mullard Radio Astronomy Observatory at Lord's Bridge, Cambridge (AMI Consortium: Zwart et al. 2008). The telescope observes in the band 13.5–17.9 GHz with eight 0.75 GHz bandwidth channels. In practice, the two lowest frequency channels (1 and 2) are not generally used due to a lower response in this frequency range and interference from geostationary satellites. The data in this paper were taken with the AMI-LA.

AMI-LA data reduction has been described extensively in previous works (see e.g. AMI Consortium: Zwart et al. 2008). For this work, flux (primary) calibration is performed using short observations of 3C 48 and 3C 147. From other measurements, we find the flux calibration is accurate to better than 5 per cent (AMI Consortium: Scaife et al. 2008; AMI Consortium: Hurley-Walker et al. 2009). Phase (secondary) calibration is carried out using interleaved observations of strong point sources (see Table 1). After calibration, the phase is generally stable to 5° for channels 4–7, and 10° for channels 3 and 8. In the following analysis, channels 4–8 have been used. We have applied an increased absolute calibration error of 10 per cent to flux densities from channel 8 in order to reflect the poorer phase stability of this channel relative to the others.

Reduced data were imaged using the AIPS data package, and CLEAN deconvolution was performed using the task IMAGR. The half power point of the AMI-LA primary beam is ≈6 arcmin at 16 GHz, and in what follows we use the convention $S_\nu \propto \nu^\alpha$, where S_ν is flux density, ν is frequency and α is the spectral index. All errors quoted are 1σ.

3 RESULTS

Flux densities were recovered from both the combined frequency data and the individual frequency channels. The combined frequency image is made in the same manner as the individual channel images, from the weighted combination of multichannel visibility data. Star-forming regions such as the Taurus molecular cloud often display complex emission structures in the radio, and consequently the data were mapped to identify possible confusion with neighbouring sources. In the cases where targets are point-like and isolated (IRAS 04016+2610, IRAS 04361+2547, IRAS 04302+2247 and IRAS 04325+2402), flux density estimates from the maps were clarified by direct fits to the visibility data; these values were found to deviate by <5 per cent.

Six of the seven target sources were detected in the continuum data, the exception being IRAS 040248+2612. IRAS 04302+2247 was detected in the continuum data, but at too low significance to recover reliable detections at >5σ in the individual channels. The remaining five objects were all detected at >5σ in at least four channels (see Table 2).

Table 2. Measured and derived properties of the AMI-LA Class I Taurus sample. Column 1: source name; columns 2–6: measured flux densities at cm wavelengths; column 7: flux density from the AMI-LA combined channel data; column 8: spectral index across the AMI-LA band.

Name	Freq. (GHz)						S_{16}	α_{AMI}
	8.44[a] (μJy)	14.62 (μJy)	15.37 (μJy)	16.12 (μJy)	16.87 (μJy)	17.63 (μJy)	(μJy)	
IRAS 04016+2610	343 ± 33	528 ± 57	555 ± 57	510 ± 46	563 ± 44	615 ± 65	546 ± 36	0.65 ± 0.27
DG Tau B	–	523 ± 49	555 ± 45	595 ± 52	645 ± 60	735 ± 78	647 ± 42	1.79 ± 0.27
IRAS 04248+2612	<100	–	–	–	–	–	<125	–
IRAS 04302+2247	160 ± 33	–	–	–	–	–	249 ± 28	–
IRAS 04325+2402	<100	148 ± 52	456 ± 50	299 ± 44	327 ± 57	<345	338 ± 28	1.49 ± 1.10
IRAS 04361+2547	140 ± 32	382 ± 49	435 ± 36	504 ± 39	–	690 ± 90	449 ± 37	2.82 ± 0.72
IRAS 04368+2557	810 ± 30[b]	918 ± 62	1040 ± 62	1194 ± 60	1014 ± 71	1151 ± 130	904 ± 54	1.17 ± 0.42

[a]8.44 GHz flux densities from Lucas, Blundell & Roche (2000).
[b]8.5 GHz flux density from Melis et al. (2011).

3.1 Spectral indices and dust disc masses

Where possible, power-law spectral indices were fitted to the AMI-LA channel data for each object (see Table 2) using the Markov chain Monte Carlo (MCMC) based maximum likelihood algorithm METRO (Hobson & Baldwin 2004). The resulting spectra were all found to be steeply rising with frequency, with a weighted average spectral index $\bar{\alpha} = 1.30 \pm 0.63$. Such steeply rising spectra are compatible with free–free emission, which has a maximum slope of $\alpha = 2$ in the optically thick regime. The presence of purely optically thick free–free emission across the AMI-LA band would imply the presence of ultra- or hypercompact H II, for which a spectral index of $\alpha \approx 1$ is typical. However, both of these are more usually associated with the later stages of more massive star formation.

Spectral indices with $\alpha > 2$, such as that measured for IRAS 04361+2546, are consistent with the slope of the SED produced by thermal emission from dust grains. In the Rayleigh–Jeans region, the opacity of the thermal emission from dust grains can be well approximated by a power law, $\kappa_\nu \propto \nu^\beta$. This index β is related to the spectral index of flux density measurements, here defined as $S_\nu \propto \nu^\alpha$, as $\beta \simeq (1 + \Delta) \times (\alpha - 2)$, where Δ is the ratio of optically thick to optically thin emission. This ratio has been previously determined in the region 350 μm to 1.3 mm as $\Delta \simeq 0.2$ (Rodmann et al. 2006; Lommen et al. 2007); however, we here assume that for much longer cm wavelengths $\Delta \to 0$, and that the emission is entirely optically thin. If the emission at 1.8 cm is entirely due to thermal dust, then the measured $\bar{\alpha}$ would imply values of $\beta \leq 0$. Although negative values of β are unphysical, values *approaching* zero are proposed for the long-wavelength tail of the greybody spectrum from young stellar objects (e.g. Pollack et al. 1994). Such values are low compared with the canonical value for the interstellar medium of $\beta_{ISM} \approx 1.8$, due to the assumed change in response to the grain size distribution within the dust population, with larger dust grains producing shallower opacity indices. Indeed, for grains with a size distribution $dn/da \propto a^{-p}$, where the grain size $a \leq a_{max}$ and $a_{max} \geq 3\lambda$, with λ the wavelength of observation, the measured opacity index $\beta(\lambda) \approx (p - 3)\beta_{ISM}$. For a typical power-law index of $p = 3.5$, grains with $\beta_{ISM} \approx 2$ will have $\beta \approx 1$ when $a_{max} > \lambda$; and by extension $\beta \leq 1$ when $a_{max} > 3\lambda$ (Draine 2006). Consequently, opacity indices of $\beta \leq 1$ indicate the largest grains, which are expected to exist as a consequence of grain growth in protoplanetary discs. Furthermore, power-law indices for grain size distributions as low as $p = 3$ have been determined in protoplanetary discs (e.g. Tanaka, Himeno & Ida 2005), reducing the expected observable value of β even further. Indeed, AW05 determined an average $\bar{\beta} =$

0.06 ± 0.02 in the wavelength range 450–850 μm consistent with these predictions, and $\beta < 0$ in the range 850 μm to 1.3 mm, the unphysical nature of which they attributed to contamination of the 1.3 mm data by alternative radio emission mechanisms, a possibility made likely by the spread in protostellar class across their much larger sample.

3.2 Spectral energy distributions

For each object in this sample, we use data at $12 \leq \lambda \leq 1300\,\mu$m from Gramajo et al. (2010) and the SED fitting tool of Robitaille et al. (2007) to fit the submm SED. This tool fits SEDs based on a gridded χ^2 procedure with the option of 200 000 SED models, composed of 20 000 radiative transfer models (Whitney et al. 2003) viewed at a range of 10 inclination angles. Each SED has contributions from a number of components including the central star itself, the envelope and the disc, the contribution from each of which will vary according to evolutionary stage as indicated by the data.

Since these SEDs are restricted to $\lambda \leq 1300\,\mu$m, we make the assumption that the dust SED is dominated at long wavelengths by the contribution from large grains predominantly found in the disc. We therefore extrapolate the disc component of the best-fitting Robitaille et al. (2007) SED as a power law with a spectral index denoted α' (to distinguish it from the low-frequency power-law index, α) from $\lambda = 1300\,\mu$m to the AMI passband to investigate whether the AMI-LA data are consistent with the tail of the greybody spectrum. Under an assumption of optically thin emission at cm wavelengths, this index is assumed to be related to the opacity index as $\beta' = \alpha' - 2$. In summary, data in the cm to submm wavelength range are consequently fitted using a double power law with low-frequency data dominated by emission with index α and higher frequency emission dominated by emission with index α'. The resulting SEDs are discussed for each object in the following section.

3.2.1 IRAS 04016+2610

Lucas, Blundell & Roche (2000, hereafter LBR2000) previously detected IRAS 04016+2610 at 3.5 and 2 cm, and placed a 3σ upper limit on the 6 cm flux density from IRAS 04016+2610 of $S_{4.89\,GHz} < 260\,\mu$Jy. However, they qualified this non-detection as an effect of the high spatial resolution of their MERLIN observations as demonstrated by a lower spatial resolution detection by Rodríguez et al. (1989) with $S_{4.89\,GHz} = 500 \pm 50\,\mu$Jy. The measured flux densities from the detections at these frequencies imply a radio
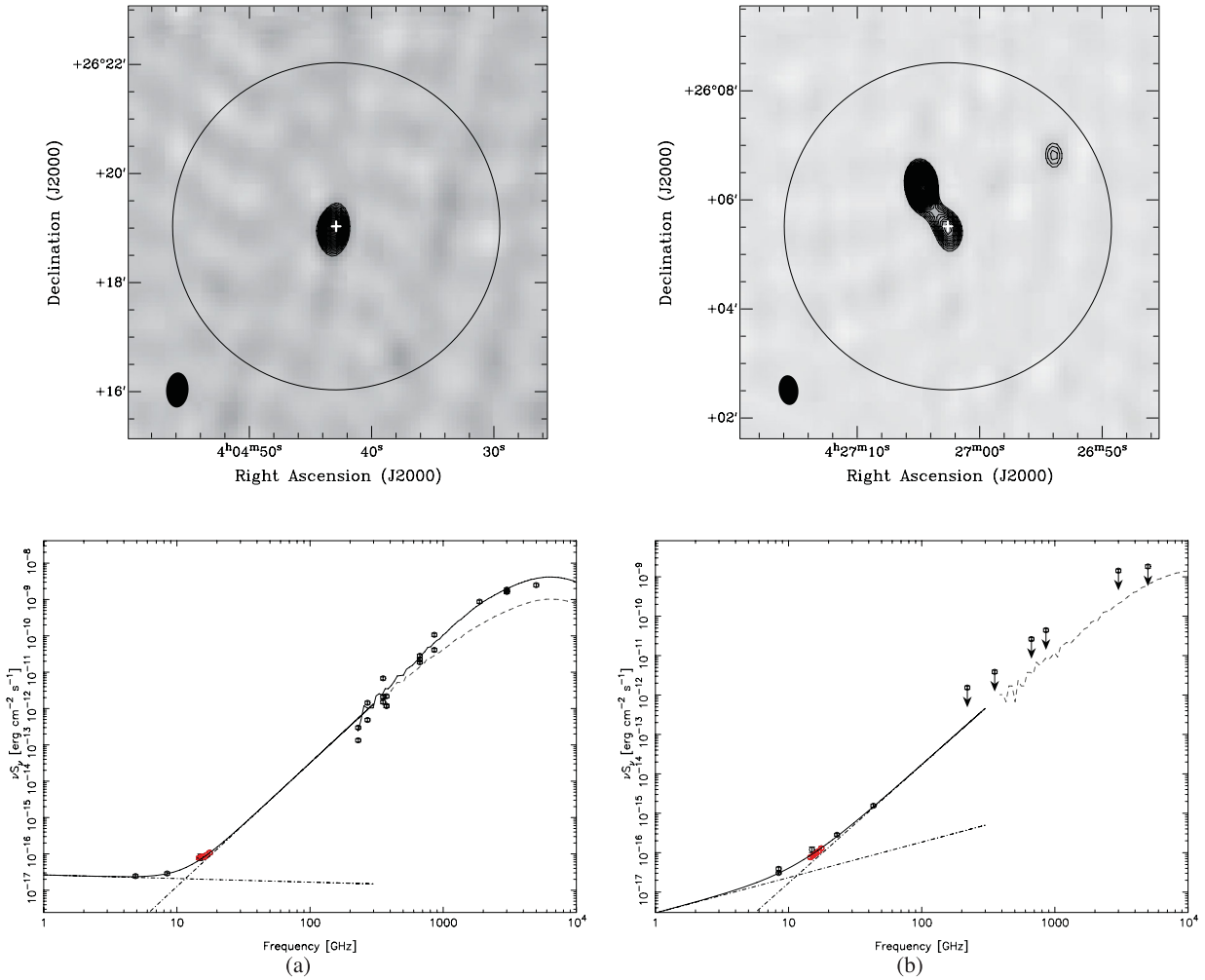
Figure 1. Top: AMI-LA 1.8 cm maps of (a) IRAS 04016+2610 and (b) DG Tau B. Contours are shown in increments of σ from 5σ, where σ for each object is listed in Table 1. The position of the target object is indicated by a white cross ('+'), the full width at half-maximum (FWHM) of the AMI-LA primary beam by a circle, and the synthesized beam is shown as a filled ellipse in the bottom left corner of each map. These maps are uncorrected for primary beam attenuation. Bottom: SEDs for (a) IRAS 04016+2610 and (b) DG Tau B. Data points at $\nu > 200$ GHz are taken from Gramajo et al. (2010), data points at lower frequencies are compiled from the literature (see text for details) and this work (see Table 2), with data from the AMI-LA indicated in red in the online version. A best-fitting SED from the grid models of Robitaille et al. (2007) is shown as a solid line at $\nu > 200$ GHz, with the disc component of this model shown as a dashed line. Below $\nu = 300$ GHz, this disc component is extrapolated as a power law (see text for details) and shown as a dot–dashed line. A second power-law spectrum is shown fitted to lower frequency radio data at $\nu < 10$ GHz with $\alpha = -1.1$ and $\alpha = -0.1$ for IRAS 04016+2610 and DG Tau B, respectively. The combined spectrum from the two power-law components is shown as a solid line at $\nu < 300$ GHz.

spectrum with $\alpha_{4.89}^{8.44} = -0.69 \pm 0.70$, suggesting a non-thermal emission mechanism. The 2 cm flux density of $S_{15\,GHz} = 700 \pm 100\,\mu$Jy from Rodríguez et al. (1989) is broadly consistent with that measured by the AMI-LA, and that of LBR2000: $S_{15\,GHz} = 520 \pm 40\,\mu$Jy. The wider cm-wave spectrum incorporating all these data (see Fig. 1a) may be fitted assuming a dominant contribution to the SED with $\alpha < -1.1$ at $\nu < 10$ GHz, above which frequency the greybody tail from thermal dust emission becomes dominant. We find a best-fitting extrapolation to the disc SED with $\alpha' = 2.4$ ($\beta' = 0.4$) (see Fig. 1a). At face value, these spectral indices imply an SED where a non-thermal emission mechanism is dominant at low radio frequencies.

Synchrotron emission would be unusual in the vicinity of proto-stellar objects as it requires both high magnetic field strengths and a population of ultrarelativistic particles. A spectral index of $\alpha = -1.1$ is broadly consistent with gyrosynchrotron emission from a quasi-relativistic power-law population of electron plasma, which

is expected to exhibit steeply falling spectral indices (Dulk 1985). Gyrosynchrotron has been invoked as a potential radio emission mechanism for a number of protostellar objects (e.g. Ray et al. 1997). The position of the peak in the spectrum of such emission is a strong function of the magnetic field strength. A spectrum which peaks below 10 GHz, such as that of IRAS 04016+2610, is likely to arise from a magnetic field with a magnitude $\sim$10 G. The magnetic field strength on the surface of Class I objects is thought to be of the order of 10^3 G, as seen towards the Class I object WL 17 (Johns-Krull et al. 2009); a field strength two orders of magnitude smaller is expected from the inner radius of the circumstellar disc (Donati & Landstreet 2009) and this may be the source of the gyrosynchrotron emission suggested here.

3.2.2 DG Tau B

A variable free–free component is suggested by the SED of DG Tau B (see Fig. 1b). The magnitude of the emission measured with
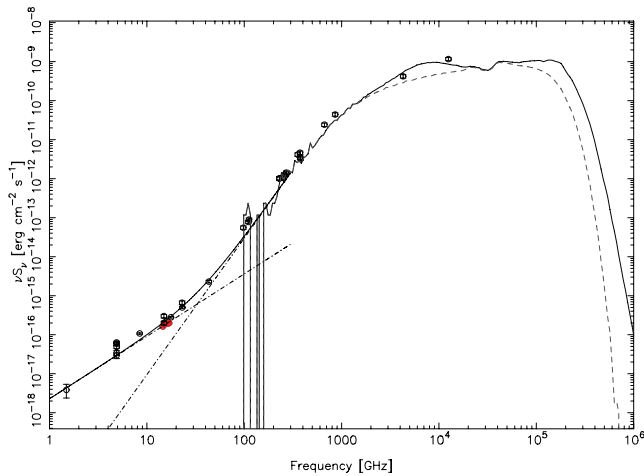
Figure 2. SED of DG Tau A. Millimetre and submm data are taken from the literature (see text for details), archival cm radio data from Wendker (1995) are shown, with data points from the AMI-LA (this work) indicated in red in the online version. A best-fitting model from the Robitaille et al. (2007) grid is shown as a solid line with the disc component indicated as a dashed line. Below 300 GHz, this disc component extrapolated as a power law with $\alpha' = 2.5\,(\beta' = 0.5)$ and a free–free component with $\alpha = 0.6$ are shown as dot–dashed lines. The combined spectrum from the two power-law components is shown as a solid line.

the AMI-LA is only ≈ 70 per cent of that measured previously by Rodríguez et al. (1996), who found $S_{15\,\mathrm{GHz}} = 0.8 \pm 0.1$ mJy for this source (see Fig. 1b), although the data are consistent within 3σ. Variability is also evident in the spectrum of the nearby source DG Tau A, which lies immediately to the north-east of DG Tau B. The spectrum for this object is presented in Fig. 2, where the spread in measurements at 5 GHz illustrates the degree of variability.

The submm to mm SED of DG Tau B is poorly constrained due to its proximity to DG Tau A; however, we find that the spectrum at frequencies $\nu > 20\,\mathrm{GHz}$ can be well described by a power law with $\alpha = 2.0\,(\beta \approx 0.0)$. This would imply a disc component with emission approximately one order of magnitude higher than that of the best-fitting grid SED found by Gramajo et al. (2010) and that the disc contribution is significant in DG Tau B. We illustrate this scaled disc model as a dashed line in Fig. 1(b).

Unlike the Class I sources targeted by this sample, DG Tau A can be seen to possess a more shallowly rising spectrum in the cm to mm-wave regime. This spectrum is nominally well fitted by an index of $\alpha = 0.6$ (see Fig. 2), the canonical value for partially optically thick free–free emission from a spherical stellar wind (Panagia & Felli 1975; Reynolds 1986). DG Tau A is a Class II source with a well-known wide-tailed molecular outflow, thought to host a large disc wind (Agra-Agoade et al. 2009), which may be providing the source of this emission. Radio flux densities for this source are taken from the catalogue of Wendker (1995). We do not include DG Tau A in our wider analysis as it is not a member of the original sample.

3.2.3 IRAS 04248+2612

IRAS 04248+2612 is a non-detection at 1.8 cm, which constrains an extrapolation of the greybody spectrum to having a spectral index $\alpha' > 2.7\,(\beta' > 0.7)$ (see Fig. 3a).

3.2.4 IRAS 04302+2247

IRAS 04302+2247 is detected at $>5\sigma$ in the AMI-LA continuum data only and it is therefore not possible to measure a spectral index at cm wavelengths directly from the AMI-LA data. Previously, it was also detected at 8.44 GHz by LBR2000, who did not detect it at 2 or 6 cm. Assuming that the detection at 8.44 GHz represents the contribution of an optically thin free–free emission component, we fit the spectrum shown in Fig. 3(b). Assuming a canonical optically thin spectral index of $\alpha = -0.1$ for the free–free component, this model is compatible with the AMI-LA continuum data point assuming an extrapolation of the best-fitting disc component to the SED with a spectral index $\alpha' = 2.3\,(\beta' = 0.3)$. However, we note that the low-frequency spectral parameters for this object remain largely unconstrained by these data.

3.2.5 IRAS 04325+2402

The AMI-LA image of IRAS 04325+2402 is dynamic range limited by the bright radio source at the half power point of the primary beam in the north-east of this field (see Fig. 4a). We tentatively associate this source with the emission-line star Coku Tau 3. As a result, the data, and hence image quality per channel, for this source are comparatively poorer than remainder of the sample and there is increased scatter in the cm-wave spectrum. This is reflected in a much larger uncertainty on the cm-wave spectral index. We find that the cm-wave flux density can be accounted for entirely by an extrapolation of the best-fitting disc component from the Robitaille et al. (2007) model with $\alpha' = 2.1\,(\beta' = 0.1)$. This conclusion is also supported by a non-detection of this object at 8.44 GHz by LRB2000.

3.2.6 IRAS 04361+2547

IRAS 04361+2547 (see Fig. 3) is found to have a steeply rising spectrum across the AMI band with $\alpha_{\mathrm{AMI}} = 2.82 \pm 0.72$. Such a spectrum is too steep to be attributed to free–free emission; however, it is similar to that found for IRAS 16293$-$2422B (Rodríguez et al. 2005).

IRAS 04361+2547 was previously detected in the radio at 4.89 GHz (Terebey, Vogel & Myers 1992) and at 8.44 GHz by LBR2000 who also made a tentative detection at 2 cm. With a measured flux density of $S_{4.89\,\mathrm{GHz}} = 230 \pm 36\,\mu\mathrm{Jy}$ (Terebey et al. 1992), a steeply falling spectral index is found below 10 GHz with $\alpha_{4.89}^{8.44} = -0.92 \pm 0.47$. Such a spectrum implies a non-thermal emission process such as synchrotron emission; however, this would be unusual for a protostellar object. Indeed, when considered as part of the wider cm-wave SED, for this emission to be compatible with that seen at 16 GHz by the AMI-LA it must possess a spectrum with $\alpha < -3.5$ (see Fig. 4b). As described previously, such a spectral index would be typical of gyrosynchrotron emission from a power-law population of electrons; it is also not incompatible with that of thermal gyrosynchrotron emission, which can have an even more steeply inverted spectrum with $\alpha_{\mathrm{TH}} = -8$.

The inference of a non-thermal emission mechanism from the SED does not take account of any possible variable free–free emission from these objects. The observations at 4.89 and 8.44 GHz were taken 7 years apart, and over a decade prior to those of the AMI-LA. Variable radio emission has been observed from a variety of protostellar objects (e.g. Shirley et al. 2007) and it is not certain that spectral behaviour determined from non-simultaneous measurements in this region of the spectrum can be relied upon.
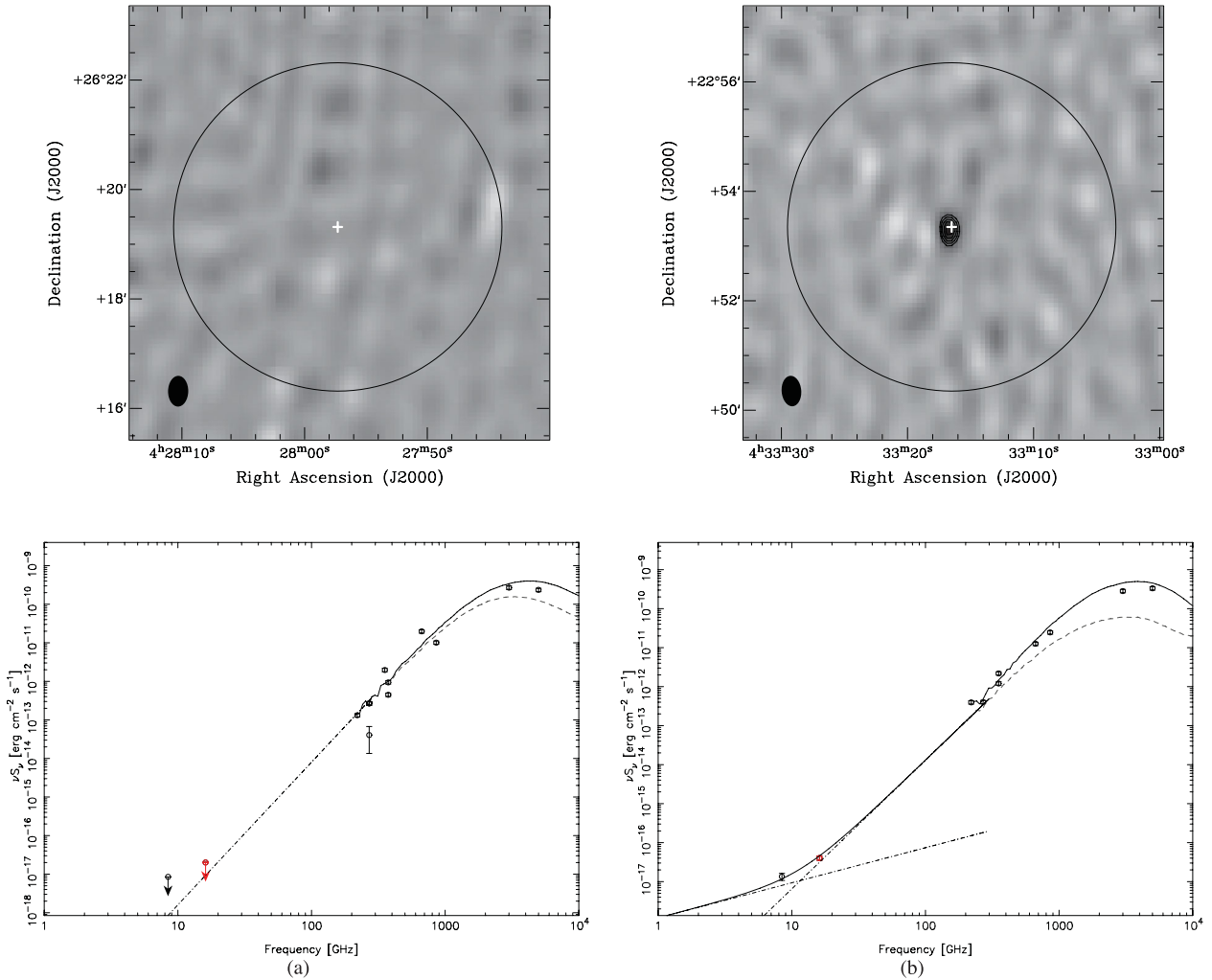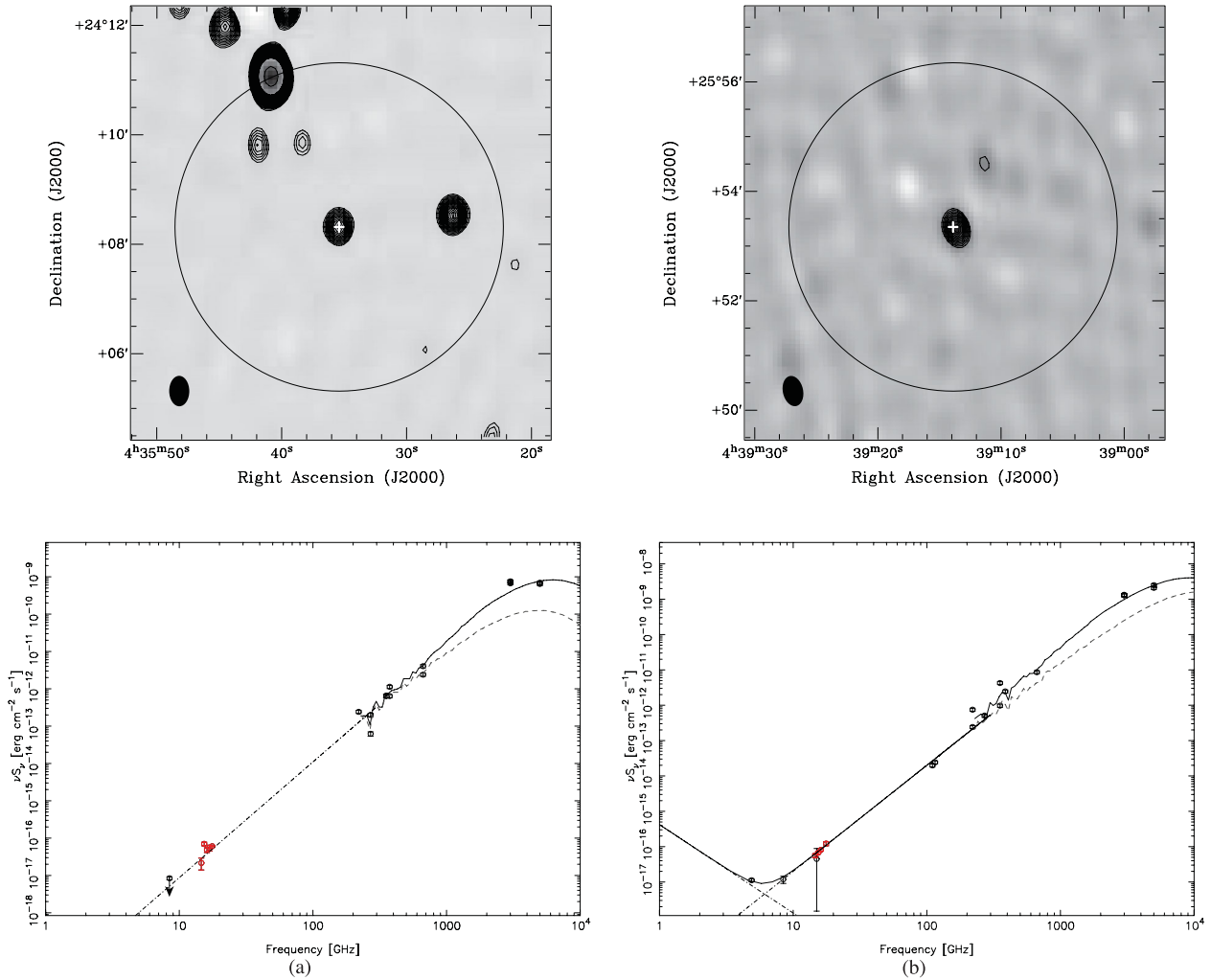
Figure 3. Top: AMI-LA 1.8 cm maps of (a) IRAS 04248+2612 and (b) IRAS 04302+2247. Contours are shown in increments of σ from 5σ, where σ for each object is listed in Table 1. The position of the target object is indicated by a white cross ('+'), the FWHM of the AMI-LA primary beam by a circle, and the synthesized beam is shown as a filled ellipse in the bottom left corner of each map. These maps are uncorrected for primary beam attenuation. Bottom: SEDs for (a) IRAS 04248+2612 and (b) IRAS 04302+2247. Data points at $\nu > 200$ GHz are taken from Gramajo et al. (2010), data points at lower frequencies are compiled from the literature (see text for details) and this work (see Table 2), with data from the AMI-LA indicated in red in the online version. A best-fitting SED from the grid models of Robitaille et al. (2007) is shown as a solid line at $\nu > 200$ GHz, with the disc component of this model shown as a dashed line. Below $\nu = 300$ GHz, this disc component is extrapolated as a power law (see text for details) and shown as a dot–dashed line. A second power-law spectrum is shown fitted to lower frequency radio data at $\nu < 10$ GHz with $\alpha = -0.1$ for IRAS 04302+2247. The combined spectrum from the two power-law components is shown as a solid line at $\nu < 300$ GHz.

We note that the tentative detection at 2 cm of IRAS 04361+2547 by LBR2000 is broadly consistent with the AMI-LA flux densities (albeit at low significance, $<4.5\,\sigma$), and was made at a similar epoch to that at 8.44 GHz which can also be accounted for by an extrapolation of the AMI-LA power law. This may imply that the spectral behaviour of IRAS 04361+2547 was similar at the LBR2000 epoch to that of the AMI-LA, but different at the epoch of the 4.89 GHz observations. Data at frequencies >5 GHz can be accounted for by an extrapolation of the greybody tail using a power law with $\alpha' = 2.0\,(\beta' = 0.0)$, and this is illustrated in Fig. 4(b).

3.2.7 IRAS 04368+2557

IRAS 04368+2557 is defined by Gramajo et al. (2010) as a borderline Class 0/I object and this is evident from the enhanced envelope contribution to its SED compared with the other sources

in this sample (see Fig. 5). This object is also part of the EVLA survey of edge-on protoplanetary discs (Melis et al. 2011), which provides flux density measurements for this source at 5, 8.5, 22.5 and 43.3 GHz. These data are combined with the new AMI-LA measurements presented here and are shown in Fig. 5. Melis et al. (2011) fitted data at $\nu \leq 8.5$ GHz and >8.5 GHz separately and constrained the low-frequency radio emission to have a spectral index of $\alpha_5^{8.5} = 0.33 \pm 0.17$ and the high-frequency emission to have an index of $\alpha_{\nu > 8.5} = 2.87 \pm 0.17$. In this work, we fit data from 5 to 350 GHz jointly using the sum of two power laws. There is a degeneracy between the fitted indices and, using MCMC sampling to explore this degeneracy, we find that the maximum likelihood spectral indices are $\alpha = -0.11 \pm 0.09$ and $\alpha' = 2.32 \pm 0.04$, where (as previously in this work) α and α' represent the spectral indices of power laws which dominate at low frequency and high frequency, respectively. A spectral index of $\alpha = -0.11$ is typical of optically thin free–free emission. Melis et al. (2011) define

© 2012 The Authors, MNRAS **420**, 3334–3343
Monthly Notices of the Royal Astronomical Society © 2012 RAS

Figure 4. Top: AMI-LA 1.8 cm maps of (a) IRAS 04325+2402b and (b) IRAS 04361+2547. Contours are shown in increments of σ from 5σ, where σ for each object is listed in Table 1. The position of the target object is indicated by a white cross ('+'), the FWHM of the AMI-LA primary beam by a circle, and the synthesized beam is shown as a filled ellipse in the bottom left corner of each map. These maps are uncorrected for primary beam attenuation. Bottom: SEDs for (a) IRAS 04325+2402b and (b) IRAS 04361+2547. Data points at $\nu > 200$ GHz are taken from Gramajo et al. (2010), data points at lower frequencies are compiled from the literature (see text for details) and this work (see Table 2), with data from the AMI-LA indicated in red in the online version. A best-fitting SED from the grid models of Robitaille et al. (2007) is shown as a solid line at $\nu > 200$ GHz, with the disc component of this model shown as a dashed line. Below $\nu = 300$ GHz, this disc component is extrapolated as a power law (see text for details) and shown as a dot–dashed line. In the case of IRAS 04361+2547, a second power-law spectrum is also shown fitted to lower frequency radio data at $\nu < 10$ GHz with $\alpha = -3.5$. The combined spectrum from the two power-law components is shown as a solid line at $\nu < 300$ GHz.

IRAS 04368+2557 as a Class 0 object and a free–free component would not be unusual for Class 0 objects which predominantly have radio counterparts. We find an opacity index $\beta' \approx \alpha' - 2 = 0.32 \pm 0.04$ substantially shallower than that of Melis et al. (2011), and consistent with the presence of large dust grains, or pebbles, in the disc.

4 DISCUSSION

4.1 Spectral indices

Using submm data to derive both opacity indices and disc masses is common practice; however, these values are uncertain due to both the approximately linear dependency on dust temperature, T_d, and also the potentially significant fraction of the submm emission that is optically thick. Perhaps, more importantly, at shorter wavelengths the measured emission cannot be exclusively attributed to the disc

alone and may be contaminated by the protostellar envelope. Measuring the emission at longer wavelengths reduces the effect of at least two of these issues significantly as the optically thick portion of the emission will be significantly reduced, if not negligible, by cm wavelengths, and additionally at frequencies below ≈ 300 GHz the disc component will be expected to dominate the SED in the majority of cases.

Consequently, although the collisional growth of dust grains in the discs around young stars has been inferred from submm observations, it is preferable to measure its properties directly from longer wavelength observations. The theoretically determined values of the opacity index for populations of these large grains ($\beta \leq$ 1; Miyake & Nakagawa 1993; Dullemond & Dominik 2005) are consistent with those measured from the cm spectrum of the objects in this sample. In the majority of cases for this sample, the contribution of additional radio emission mechanisms at 1.8 cm has found to be subdominant with ≥ 70 per cent of the flux density attributable
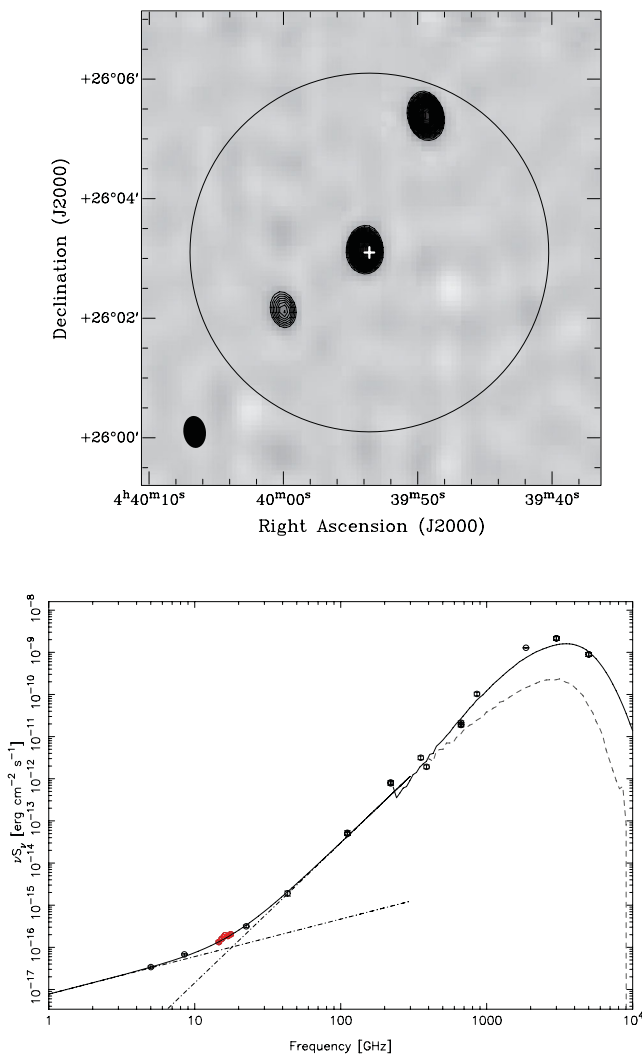
Figure 5. Top: AMI-LA 1.8 cm map of IRAS 04368+2557. Contours are shown in increments of σ from 5σ, where σ is listed in Table 1. The position of the target object is indicated by a white cross ('+'), the FWHM of the AMI-LA primary beam by a circle, and the synthesized beam is shown as a filled ellipse in the bottom left corner of the map. This map is uncorrected for primary beam attenuation. Bottom: SED for IRAS 04368+2557. Data points at $\nu > 200$ GHz are taken from Gramajo et al. (2010), data points at lower frequencies are compiled from the literature (see text for details) and this work (see Table 2). A best-fitting SED from the grid models of Robitaille et al. (2007) is shown as a solid line at $\nu > 200$ GHz, with the disc component of this model shown as a dashed line. Below $\nu = 300$ GHz, this disc component is extrapolated as a power law (see text for details) and shown as a dot–dashed line. A power-law radio spectrum is also shown fitted to lower frequency radio data at $\nu < 10$ GHz with $\alpha = -0.11$ (see text for details).

to thermal dust emission. IRAS 04368+2557 is an exception to this with only 20 per cent of the 1.8 cm emission coming from thermal dust. This is notable as IRAS 04368+2557 is the only object in this sample which is Class 0, rather than Class I. This lack of free–free emission in the wider sample is of particular note as such emission in young stellar objects is often attributed to the presence of a molecular outflow, with shock ionization in the outflow proposed to be the source of the ionized plasma giving rise to the free–free emission. All the objects within this sample are known

Table 3. Opacity indices and disc masses for the sample. Column 1 lists the target name; column 2 the spectral index measured from AMI-LA data alone; column 3 the spectral index dominant at low frequencies from the joint power-law fit; column 4 the spectral index dominant at higher frequencies from the joint power-law fit; column 5 the opacity index corresponding to the high-frequency power law; column 6 the flux density predicted by the high-frequency power law at 1.8 cm; column 7 the disc mass calculated from the flux density in column 6 assuming the opacity index β'; column 7 the disc mass calculated from the flux density in column 6 assuming an opacity index of $\beta = 1$.

Name	$\alpha_{\rm AMI}$	α	α'	β'	$S_{\rm pred,16}$ (μJy)	$M_{\rm disc}$ $\beta = \beta'$ ($M_\odot$)	$\beta = 1$ ($M_\odot$)
IRAS 04016+2610	0.65	−1.1	2.4	0.4	399	0.013	0.150
DG Tau B	1.79	−0.1	2.0	0.0	442	0.003	0.166
IRAS 04248+2612	–	–	2.7	0.7	<125	<0.012	<0.047
IRAS 04302+2247	–	−0.1	2.3	0.3	181	0.004	0.068
IRAS 04325+2402	1.49	–	2.1	0.1	238	0.002	0.089
IRAS 04361+2547	2.82	−3.5	2.0	0.0	449	0.003	0.168
IRAS 04368+2557	1.17	−0.1	2.3	0.3	174	0.004	0.065

to possess molecular outflows (Gramajo et al. 2010); however, as has been observed in larger samples of Class 0 and I objects, the detection rate at cm wavelengths for Class I sources ($\approx$20 per cent) is significantly lower than that of Class 0 sources ($\approx$70 per cent; AMI Consortium: Scaife et al. 2011). However, we note that the contribution of both thermal and non-thermal emission in young stellar objects appears to be variable (e.g. Shirley et al. 2007) as indicated by the discrepant flux densities at radio frequencies from observations at different epochs in the literature.

Extrapolating power-law SEDs from the submm to the AMI-LA waveband requires shallow spectral indices of $\alpha = 2.0$–2.7, with an average value of $\bar{\alpha} = 2.26$ corresponding to $\bar{\beta} = 0.26 \pm 0.22$. These indices are consistent with grain growth in these objects providing a population of larger dust grains or *pebbles*. Such dust populations, with grains exceeding cm sizes (Draine 2006), have been theoretically demonstrated to have opacity indices approaching zero (Miyake & Nakagawa 1993; Draine 2005; Dullemond & Dominik 2005) and the SEDs for the sample presented in this work support these predictions.

4.2 Disc masses

Using the SED fits to the radio and submm data, we can separate the contributions from high-frequency dust emission and low-frequency radio emission at 1.8 cm. The contribution of the thermal dust emission at this wavelength is listed for each source in Table 3. Making the assumption that all dust emission at this wavelength will be optically thin, we calculate disc masses using

$$M_{\rm disc} = \frac{S_\nu d^2}{\kappa_\nu B_\nu(T_{\rm d})}. \tag{1}$$

We use a dust temperature of $T_{\rm d} = 20$ K, the characteristic temperature found by AW05 at 1.3 mm. We note that increasing the value of $T_{\rm d}$ to that of 60 K assumed by Terebey et al. (1992) at 2.7 mm would decrease our derived mass values by a factor of $\approx$3. As well as temperature, the disc mass is a sensitive function of β due to its linear dependence on the opacity, κ_ν. Following Beckwith et al. (1990), we assume $\kappa_\nu = 0.1(\nu/1000\,{\rm GHz})^\beta$ cm^2 g^{-1} (a dust-to-gas ratio of 1:100). With $\beta = 1$, this leads to a value for the opacity at 1.8 cm (16 GHz) of $\kappa_{16\,{\rm GHz}} = 0.002$ cm^2 g^{-1}.

The disc mass values derived from submm data by AW05 assume a value of $\beta = 1$ when calculating the opacity. Disc mass estimates made directly from the AMI-LA flux densities under the same assumption are systematically higher than those derived from submm data (see Table 3). Drawing a comparison with the disc mass values from the best-fitting SED models of Robitaille et al. (2007) plotted in Figs 1, 2 and 5 for each source, there is a loose agreement between the submm disc mass estimates, although the scatter is large. However, the cm-wave mass estimates from the AMI-LA data are systematically higher than those derived from shorter wavelengths. One possible physical explanation for this difference is that the larger mass estimates arise as consequence of increased emission from larger dust grains at cm wavelengths through the disc. This emission does not contribute to the submm flux density, which predominantly traces smaller grains nearer to the disc surface due to optical depth effects in the disc core.

However, the disc mass estimates from the AMI-LA data using values of $\beta = \beta'$ derived from the SED fits (see Table 3) are systematically smaller than those found in AW05. This is a strong function of the lower values of the opacity index and therefore the correspondingly larger opacities. A clear example of this is IRAS 04361+2547, where the difference in calculated disc mass is over an order of magnitude. It is unclear whether the apparent difference between the submm-derived mass values and those from the AMI-LA data is real. The submm values use a value of $\beta = 1$ which is significantly larger than that derived from SED fitting in AW05, where β is found to have an average value of approximately zero, and so the submm masses could be considered to be overestimated. Conversely, the opacity index is expected to flatten towards lower frequencies and therefore the disc masses derived at cm wavelengths should probably assume lower values of β.

Similar to AW05, we find that the disc masses derived from the cm-wave flux densities assuming $\beta = 1$, although larger than those inferred from submm data, are still often significantly lower than those required by theory for giant planet formation (Pollack et al. 1996; Boss 1998). Three objects are exceptions to this: IRAS 04016+2610, DG Tau B and IRAS 04361+2547. For each of these objects, the calculated disc mass is above the limit required for planet formation of $0.13\,M_\odot$ (Boss 1998).

The gravitational instability mechanism of giant planet formation is a short-lived process and most likely to occur during the early protostellar stages, at a stellar lifetime of $\approx 10^5$ yr (Boss 1998). This lifetime is typical of Class I objects, and given the frequency of such planets observed around more evolved stellar objects, we might consequently expect that objects such as those found in this sample would in the majority have observationally measured masses compatible with such a process. As suggested by AW05, it is possible that an underestimation of the disc mass from the disc SED may arise from the presence of a population of large grains which do not contribute to the emission at submm to cm wavelengths, but which act to increase the mass of the disc. Such a situation is more likely at submm than at cm wavelengths; however, it is difficult to state that disc mass estimates from submm flux densities are universally underestimated as there will also be a competing contribution at these wavelengths from the protostellar envelope. This contribution can only be separated out using high-resolution interferometric observations. Alternatively, the core accretion mechanism of giant planet formation (e.g. Pollack et al. 1996) requires significantly longer time-scales of order 10^7 yr, allowing young stellar objects in the relatively early stages of their evolution to continue accreting mass on to their protostellar discs and consequently to increase their mass.

5 CONCLUSIONS

We have extended the SEDs of seven young stellar objects down to cm wavelengths in order to constrain that part of the spectrum dominated by their circumstellar discs. The key results from this sample are summarized as follows.

(i) We find that for the Class I objects in this sample, the emission at 1.8 cm is still dominated by the tail of the dust greybody spectrum, rather than alternative radio emission mechanisms, with 70–100 per cent of the cm-wave emission being attributable to thermal dust emission. The same is not true for IRAS 04368+2557, which is assumed to be Class 0 and has only a 20 per cent contribution from thermal dust at 1.8 cm.

(ii) We find spectral indices consistent with a flattening of the opacity index towards longer wavelengths, with an average value $\bar{\beta} = 0.26 \pm 0.22$, consistent with a significant population of large dust grains, and in accordance with theoretical models for the collisional growth of grains within circumstellar discs.

(iii) We derive disc masses directly from the thermal dust contribution to the cm-wave flux densities. Under an assumption of $\beta = 1$, following AW05 we find that these mass estimates are systematically higher than those determined from submm data. Since the average value of the opacity index from SED fitting is similar at 1.8 cm and 850 µm, we attribute this difference in disc masses to an increased emission contribution from larger dust grains within the disc at cm wavelengths. Under these assumptions, disc masses in excess of the lower limit required for giant planet formation (Boss 1998) are recovered in almost 50 per cent of the cases.

REFERENCES

Agra-Amboage V., Dougados C., Cabrit S., 2009, Tsinganos K., Ray T., Stute M., eds, Astrophys. and Space Proc. Ser., Protostellar Jets in Context. Springer, Berlin, p. 477
AMI Consortium: Hurley-Walker N. et al., 2009, MNRAS, 396, 365
AMI Consortium: Scaife A. M. M. et al., 2008, MNRAS, 385, 809
AMI Consortium: Scaife A. M. M. et al., 2011, MNRAS, 410, 2662
AMI Consortium: Zwart J. T. L. et al., 2008, MNRAS, 391, 1545
Andrews S. M., Williams J. P., 2005, ApJ, 631, 1134 (AW05)
Beckwith S. V. W., Sargent A. I., 1993, ApJ, 402, 280
Beckwith S. V. W., Sargent A. I., Chini R. S., Guesten R., 1990, AJ, 99, 924
Boss A. P., 1998, ApJ, 503, 923
Donati J.-F., Landstreet J. D., 2009, ARA&A, 47, 333
Draine B. T., 2006, ApJ, 636, 1114
Dulk G. A., 1985, ARA&A, 23, 169
Dullemond C. P., Dominik C., 2005, A&A, 434, 971
Dutrey A., Guilloteau S., Simon M., 2003, A&A, 402, 1003
Gramajo L. V., Whitney B. A., Gómez M., Robitaille T. P., 2010, AJ, 139, 2504
Hobson M. P., Baldwin J. E., 2004, Applied Opt., 43, 2651
Johns-Krull C. M., Greene T. P., Doppmann G. W., Covey K. R., 2009, ApJ, 700, 1440

Kamp I., Dullemond C. P., 2004, ApJ, 615, 991

Lommen D. et al., 2007, A&A, 462, 211

Lucas P. W., Blundell K. M., Roche P. F., 2000, MNRAS, 318, 526 (LBR2000)

Melis C. et al., 2011, ApJ, 739, L7

Miyake K., Nakagawa Y., 1993, Icarus, 106, 20

Panagia N., Felli M., 1975, A&A, 39, 1

Pollack J. B., Hollenbach D., Beckwith S., Simonelli D. P., Roush T., Fong W., 1994, ApJ, 421, 615

Pollack J. B., Hubickyj O., Bodenheimer P., Lissauer J. J., Podolak M., Greenzweig Y., 1996, Icarus, 124, 62

Ray T. P., Muxlow T. W. B., Axon D. J., Brown A., Corcoran D., Dyson J., Mundt R., 1997, Nat, 385, 415

Reynolds S. P., 1986, ApJ, 304, 713

Robitaille T. P., Whitney B. A., Indebetouw R., Wood K., 2007, ApJS, 169, 328

Rodmann J., Henning T., Chandler C. J., Mundy L. G., Wilner D. J., 2006, A&A, 446, 211

Rodríguez L. F., Myers P. C., Cruz-Gonzalez I., Terebey S., 1989, ApJ, 347, 461

Rodríguez L. F., Anglada G., Raga A., 1995, ApJ, 454, L149

Rodríguez L. F., Loinard L., D'Alessio P., Wilner D. J., Ho P. T. P., 2005, ApJ, 621, L133

Shirley Y. L., Claussen M. J., Bourke T. L., Young C. H., Blake G. A., 2007, ApJ, 667, 329

Shirley Y. L., Huard T. L., Pontoppidan K. M., Wilner D. J., Stutz A. M., Bieging J. H., Evans N. J., II, 2011a, ApJ, 728, 143

Shirley Y. L., Mason B. S., Mangum J. G., Bolin D. E., Devlin M. J., Dicker S. R., Korngut P. M., 2011b, AJ, 141, 39

Tanaka H., Himeno Y., Ida S., 2005, ApJ, 625, 414

Terebey S., Vogel S. N., Myers P. C., 1992, ApJ, 390, 181

Wendker H. J., 1995, A&AS, 109, 177

Whitney B. A., Wood K., Bjorkman J. E., Wolff M. J., 2003, ApJ, 591, 1049

This paper has been typeset from a TEX/LATEX file prepared by the author.